applied sciences

MDPI

Article

Study of Surface Defect Detection Techniques in Grinding of SiCp/Al Composites

Haotao Wang [1], Haijun Zhang [2], Ming Zhou [1,*], Chengbo Gu [1], Sutong Bai [1] and Hao Lin [1]

[1] School of Mechatronic Engineering, Harbin Institute of Technology, Harbin 150001, China; 18b308010@stu.hit.edu.cn (H.W.); 22s008160@stu.hit.edu.cn (C.G.); baisutong2023@163.com (S.B.); lh927175@163.com (H.L.)
[2] Research Center of Laser Fusion, China Academy of Engineering Physics, Mianyang 621900, China; sukersaha@caep.cn
* Correspondence: zhouming@hit.edu.cn

Abstract: SiCp/Al composites are used in the aerospace, automotive, and electronics fields, among others, due to their excellent physical and mechanical properties. However, as they are hard-to-machine materials, poor surface quality has become a major limitation to their wider applications. To effectively control the quality of machined surfaces, it is necessary to accurately detect and characterize defects. Based on the YOLOv4 object detection algorithm, a SiCp/Al composite machined surface defect detection model has been developed for the accurate and fast detection of machined surface defects. OpenCV is used to process images of detected defects and extract defect feature parameters. The number of defects and the total defect area in the same machining area are used as evaluation criteria to assess the quality of the machined surface, and the effect of the machining parameters on the quality of the machined surface is analyzed. The results show that the number and total area of surface defects that occur when grinding SiCp/Al composites are positively correlated with the feed rate, tool diameter, and size of the abrasive, while they are negatively correlated with the spindle speed and ultrasonic vibration amplitude. When the grinding depth is greater than 20 microns, the quality of the machined surface is greatly affected.

Keywords: SiCp/Al composites; defect detection; defect feature extraction; area of defects; surface quality

check for updates

Citation: Wang, H.; Zhang, H.; Zhou, M.; Gu, C.; Bai, S.; Lin, H. Study of Surface Defect Detection Techniques in Grinding of SiCp/Al Composites. *Appl. Sci.* **2023**, *13*, 11961. https://doi.org/10.3390/app132111961

Academic Editor: Mark J. Jackson

Received: 9 October 2023
Revised: 30 October 2023
Accepted: 1 November 2023
Published: 2 November 2023

Copyright: © 2023 by the authors. Licensee MDPI, Basel, Switzerland. This article is an open access article distributed under the terms and conditions of the Creative Commons Attribution (CC BY) license (https://creativecommons.org/licenses/by/4.0/).

1. Introduction

Silicon-carbide-particle-reinforced aluminum matrix (SiCp/Al) composites have excellent physical and mechanical properties [1]. They exhibit higher strength-to-weight ratios, hardness, stiffness, wear resistance, etc., compared to conventional metals and alloys [2]. As a result, SiCp/Al composites are widely used in the aerospace, automotive, and electronics fields, amongst others [3].

In practice, the processing quality of materials is highly demanded in various areas of precision and ultra-precision production and manufacturing. However, the addition of silicon carbide particles, while giving SiCp/Al composites excellent properties, also weakens the machinability of SiCp/Al composites [4], resulting in poor machined surface quality and the presence of various defects [5,6]. Therefore, a reduction in machined surface defects and improvements in machined surface quality are important for the further development and application of SiCp/Al composites.

Since machined surface defects directly affect machined surface quality, the accurate detection and characterization of machined surface defects is a prerequisite for the effective control of machined surface quality. With the development of computer image processing techniques, methods have emerged to obtain images using machine vision devices and to judge surface defect information in images through image processing. In the early days, defects were evaluated using only image processing and feature extraction methods,

which were poorly adapted, inefficient, and did not provide intelligent evaluation results. Therefore, a surface defect detection method combining machine vision and machine learning is proposed to replace the role played by the human brain, using machine learning to judge the presence of defects and thus transforming surface defect detection based on machine vision into automation and intelligence [7]. With improvements in the performance of deep learning, deep learning-based surface defect detection has become the dominant method for surface defect detection due to its high detection accuracy and fast detection speed [8].

Currently, deep learning-based material surface defect detection algorithms can be categorized into two-stage defect detection algorithms and single-stage defect detection algorithms according to their different structures. The two-stage defect detection algorithm first extracts the image features, obtains candidate regions based on the feature maps, and then performs a sliding-window operation on the candidate regions to obtain location and category information on the defects. Representative two-stage defect detection algorithms include R-CNN [9], SPP-Net [10], Fast R-CNN [11], Faster RCNN [12], and R-FCN [13]. The single-stage defect detection algorithm generates candidate boxes while performing classification and regression tasks, which are represented by the YOLO [14] and SSD [15] series networks.

In contrast to the two-stage defect detection algorithm, the YOLO series of algorithms uses a neural network model to implement an end-to-end training process, which is an overall framework structure with a smaller number of parameters and faster running speed. The YOLOv4 [16] algorithm can not only achieve a high level of detection accuracy compared to other versions in the YOLO series but also is faster and better able to meet the real-time detection requirements of the industrial sector. As a result, a large number of scholars have applied YOLOv4-based defect detection algorithms for detecting defects on PCBs [17], chips [18], railways [19], fabrics [20,21], transmission line insulators [22,23], etc. The results show that the proposed defect detection algorithm performs well in terms of accuracy and detection speed. However, few deep learning-based methods have been reported for surface defect detection in SiCp/Al composites. Therefore, in order to achieve the accurate detection of surface defects in SiCp/Al composites, and in view of the excellent performance of YOLOv4 in defect detection, in this paper, the YOLOv4 algorithm is used to detect defects on the ground surface of SiCp/Al composites, and a surface quality evaluation criterion is also proposed.

2. Detection Process of Surface Defects in SiCp/Al Composites

2.1. Establishment of the Image Dataset for Machined Surface Defects

Ultrasonic-vibration-assisted machining, a type of non-conventional machining, has significant advantages for difficult-to-machine materials. Therefore, ultrasonic-vibration-assisted grinding experiments on SiCp/Al composites were performed in order to obtain a dataset of surface defects in SiCp/Al composite machining and to subsequently analyze the effect of process parameters on machined surface defects on the SiCp/Al composites. Four grinding process parameters and two grinding wheel parameters were chosen as the experimental variables, and a univariate experimental approach was used, as shown in Table 1. The machine used in the experiment is a DMG Ultrasonic 70-5 linear ultrasonic machining center (DMG MORI, Bielefeld, Germany), and the workpiece material is a SiCp/Al2024 composite with a 45% volume fraction, where the average size of the SiC particles is 5 μm. Table 2 presents the mechanical properties of the Al2024 matrix and the silicon carbide particles. Considering the shock load in ultrasonic-vibration-assisted grinding, a nickel-bonded diamond grinding wheel for ultrasonic machining from SCHOOTT Diamond Tools Corp. was selected as the grinding tool. Furthermore, since the dimension of defects on machined surfaces is commonly on the micrometer scale, an ultra-deep-field microscope is used instead of a CCD camera for image acquisition. All images are 1600 × 1200 pixels in size. Figure 1 shows the whole grinding experimental setup and the machining surface image

acquisition process. The sample of the workpiece following ultrasonic-vibration-assisted grinding is shown in Figure 2.

Table 1. Process parameters for grinding of SiCp/Al composite.

Process Variables	Levels
Spindle speed n (rmp)	3000, 6000, 9000, 12,000, 15,000
Feed rate v_f (mm/min)	15, 20, 25, 30, 35
Cutting depth a_p (μm)	5, 10, 15, 20, 25
Ultrasonic vibration amplitude A (μm)	0, 1.25, 2.5, 3.75, 5
Tool Diameter d (mm)	2, 4, 6, 8
Abrasive size S_a (μm)	46, 54, 64, 76

Table 2. Material property parameters of Al2024 alloy and SiC particle.

Material Properties	Al2024	SiC Particle
Density (g/cm^3)	2.77	3.2
Young's modulus (GPa)	71	3.2
Specific heat (J/g k)	0.8875	0.427
Thermal conductivity (W/m K)	180	81
Coefficient of thermal expansion (K^{-1})	23.6×10^{-6}	4.9×10^{-6}
Poisson's ratio	0.34	0.183

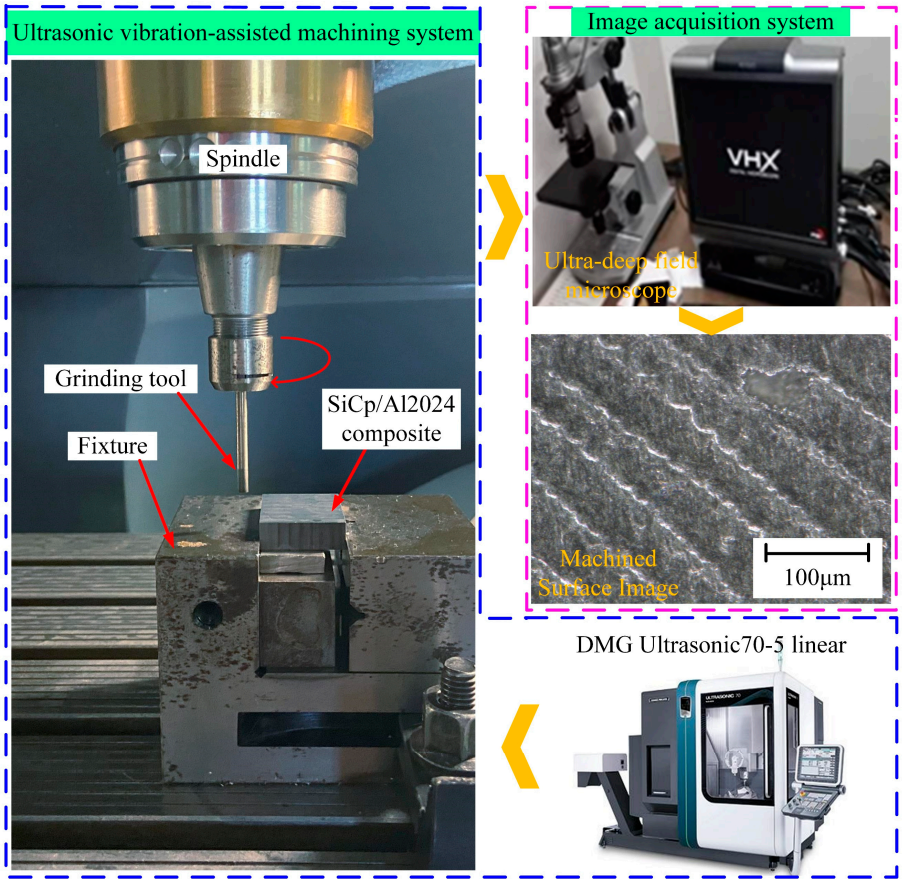


Figure 1. Grinding experimental setup and the machining surface image acquisition process.

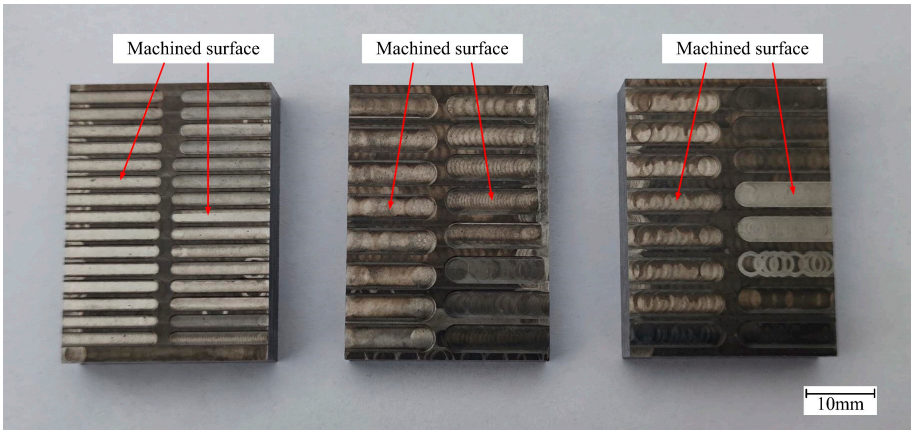


Figure 2. Workpiece after grinding machining.

Before training the surface defect detection model, the obtained surface images needed to be annotated to build the processed surface defect dataset. LABELIMG software (version 1.3.0) was used to annotate images, and a file containing the image size, defect type, and location information was generated after annotation. To enable the neural network to better learn the difference between the background and defects and to improve the detection accuracy, defect-free images were added to the dataset as negative samples. In addition, images containing oil contamination were also added to the dataset as negative samples during training to enable the model to better distinguish oil residues from machined surface defects. Some dataset images are shown in Figure 3.

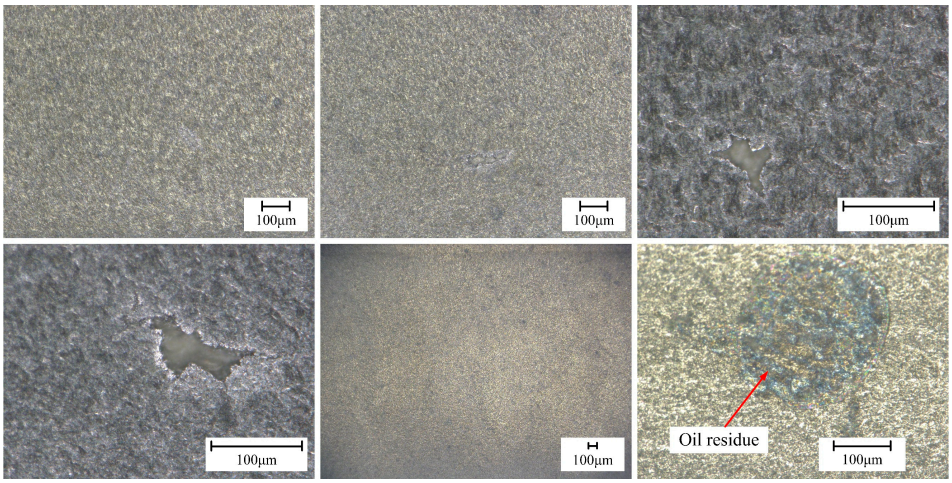


Figure 3. The images of several samples.

2.2. Detection Model for SiCp/Al Composite Surface Defects

As shown in Figure 4, YOLOv4 consists of a backbone network (CSPDarknet53), a neck network (SPP and PANet), and a predictive network (YOLOHead). The CSPDarknet53 network consists of a CBM module and a CSP module. The CSP module consists of down sampling and n residual blocks with values of 1, 2, 8, and 4 in the backbone network, respectively. The advantage of adding the CSP module is that it ensures that the amount of computation does not increase much while still obtaining a comparable network depth, and the use of skip connections mitigates the vanishing gradient problem caused by increasing network depth.

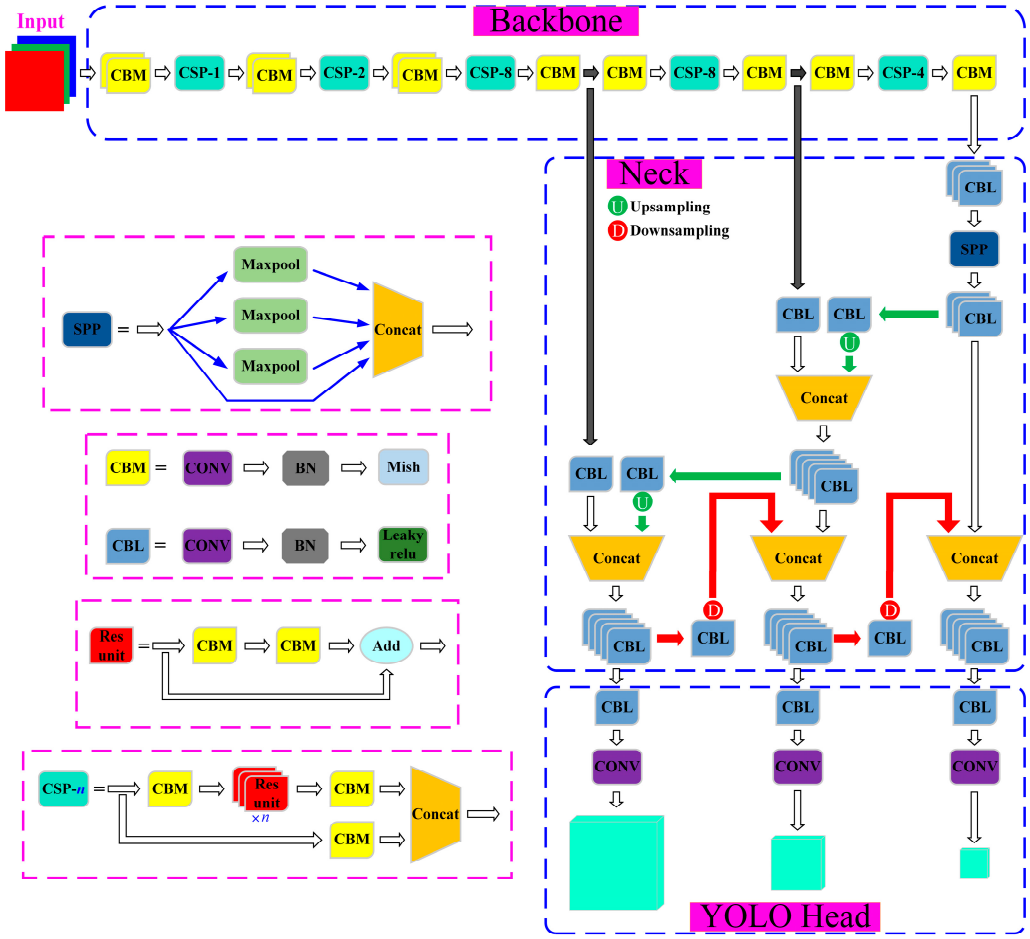


Figure 4. Structure of YOLOv4 algorithm.

The neck network consists of an SPP structure and a PANet structure. The output of CSPDarknet53 is processed with three convolutions as input to the SPP structure, and then the four pooling kernels of different sizes included in the SPP structure are used for max pooling and the pooled feature maps are concatenated as the output. The use of the SPP module increases the reception of backbone features more effectively than simply using a single-size pooling kernel for max pooling, significantly separating the most important contextual features. PANet is a combination of FPN and PAN structures. The FPN layer is able to capture strong semantic features from the top to bottom, while PAF conveys strong localization features from the bottom to top. By combining these two modules, more accurate target location information can be obtained.

YOLO-Head uses multi-scale features obtained from the PANet structure for regression and classification prediction. The scales of output feature maps in YOLO-Head are (19, 19, 18), (38, 38, 18), and (76, 76, 18), respectively. Each grid cell in the YOLOv4 output feature map contains three anchors, and each anchor contains five basic parameters (x, y, w, h, confidence) and i category parameters. Since there is only one defect category (pits), the value of i is 1. Thus, the third dimension of the feature map of YOLO-Head is 18 ($3 \times (5 + 1)$).

YOLOv4 has an initial nine anchors, each of which contains two parameters: the length and width of the anchor. In order for the detection model to learn the target locations quicker during training and thus speed up the training process, K-means clustering is employed to compute the appropriate anchor size for the defect dataset. Nine labeled boxes are randomly selected as the clustering centers of the K-means, and then the similarity between all labeled boxes and these nine clustering centers is calculated. Based on the similarity calculation, labeled boxes are assigned to different cluster centers, which are then

updated based on the average of the samples contained in each cluster center. The above steps are repeated until the clustering is complete. The values of the anchors under the different feature maps obtained through clustering are given in Table 3.

Table 3. Anchors for each feature map.

Feature Map	Anchors
76 × 76	(34, 43) (66, 79) (81, 144)
38 × 38	(153, 125) (130, 245) (234, 210)
19 × 19	(239, 351) (177, 413) (492, 227)

In addition, in order for the neural network to pay different levels of attention to the input data and perform feature extraction more effectively on the target identified, the Efficient Channel Attention (ECA) module is introduced into the defect detection model. In general, the addition of the attention module increases the complexity of the neural network and the amount of computation. The ECA module is lightweight and thus results in little increase in the number of network parameters and does not have a large impact on the complexity of the neural network. Compared with CBAM, SENet, and other modules, the ECA module can achieve better performance with a smaller number of parameters.

2.3. Training and Evaluation of Defect Detection Model

2.3.1. Environment Configuration and Evaluation Criterion

The environment configuration used for the implementation of the algorithm is as follows.

Operating system: Microsoft Windows 10; development language: Python 3.6; GPU accelerated library: CUDA 9.2 And CUDNN 7.6.2; CPU: Intel Xeon W-2255; GPU: Nvidia GeForce RTX 2080Ti 11G; RAM: 64G.

The mean average precision (mAP) is usually chosen as the evaluation criterion for detection results. The mAP is the weighted average of the average accuracy (AP) for all detection categories. The AP value is the area under the P-R curve formed by connecting points consisting of precision and recall at different confidence levels. The values of precision, recall, AP, and mAP can be obtained from Equations (1)–(4).

$$\text{Precision} = \frac{\text{TP}}{\text{TP} + \text{FP}} \tag{1}$$

$$\text{Recall} = \frac{\text{TP}}{\text{TP} + \text{FN}} \tag{2}$$

$$\text{AP} = \int_0^1 \text{P(R)}\, \text{dR} \tag{3}$$

$$\text{mAP} = \frac{1}{N} \sum_{i=1}^{N} \text{AP}_i \tag{4}$$

TP (True Positive) is the number of positive samples predicted to be positive, TN (True Negative) is the number of negative samples predicted to be negative, FP (False Positive) is the number of negative samples predicted to be positive, and FN (False Negative) is the number of positive samples predicted to be negative.

2.3.2. Training Process

A transfer learning approach is used to train defect detection models. Transfer learning is the use of existing similar datasets or already trained models for the training of a new model. A pre-trained model is obtained through some other datasets similar to the surface defect dataset, and then this pre-trained model is used to train our own dataset. Transfer

learning not only speeds up the training of the model but also increases the diversity of the dataset and the amount of data to some extent.

The acquired processed surface images were divided into training and validation sets in a 9:1 ratio. First, the training was frozen; that is, the feature extraction parameters of the backbone network were frozen with the pre-trained weights, and the learning rate was set to 0.001 iterations for 30 epochs to speed up the training process. In the unfreezing phase, the learning rate was set to 0.0001 iterations for 40 epochs and then to 0.00001 iterations for 30 epochs. Gradually decreasing the learning rate slows down the gradient descent and reduces the gradient descent step size, which makes it easier to approach the minimum point. In addition to setting different learning rates as described above, this paper also employs learning rate cosine annealing. This utilizes the idea of an annealing optimization method, using linear ascent in the ascent phase and simulated cosine function descent in the descent phase. Using the learning rate cosine annealing method, the network can avoid becoming trapped in the local optimal solution.

After the training was complete, the trained model was used to detect images in the validation set. The surface defect detection results for SiCp/Al composites at different magnifications are shown in Figure 5. It was found that regardless of the size of the defects, the detection model could detect their locations and label them with the defect types and the correct prediction probability for detection results. Since only pit defects were detected, the AP and mAP values are equal. The AP values obtained for the defect detection dataset are calculated to be 97.4%, and the average detection time per image is only 47 ms.

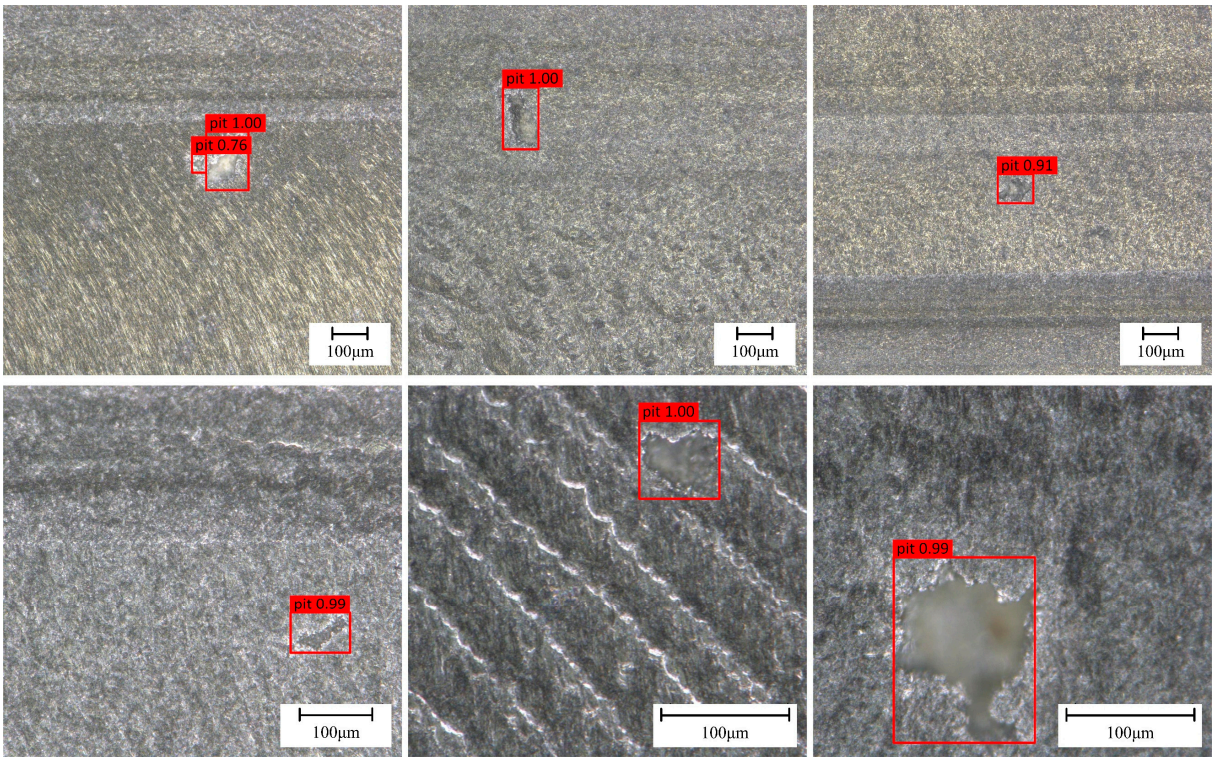


Figure 5. Surface defect detection results of SiCp/Al composites.

3. Extraction of Characteristic Parameters of Surface Defects

Based on the detection and localization of defects, OpenCV was used to perform a series of image processing tasks such as cropping, edge detection, and morphological operations on the detected defect regions to obtain surface defect feature parameters.

3.1. Edge Detection

The Canny algorithm [24] is used for edge detection. The Canny edge detection algorithm is normally divided into four steps: (1) smoothing the image using a Gaussian filter, (2) calculating the gradient value and direction of each pixel point, (3) applying non-maximum suppression to filter pixel points with small gradient values in the local region, and (4) filtering and connecting edges with a dual-threshold algorithm.

To explain the edge detection process, six detected defects on the machined surface were randomly selected and clipped using OpenCV to obtain a sample image of the defect region, as shown in Figure 6. In optical images, regions with different depths of field have different levels of sharpness. The background information is clearer and more complex, the interior of the defect is blurred, and no smoothing operation is applied, which helps distinguish the defect from the background region. Therefore, the image-smoothing operation was skipped, and gradient computation was performed directly.

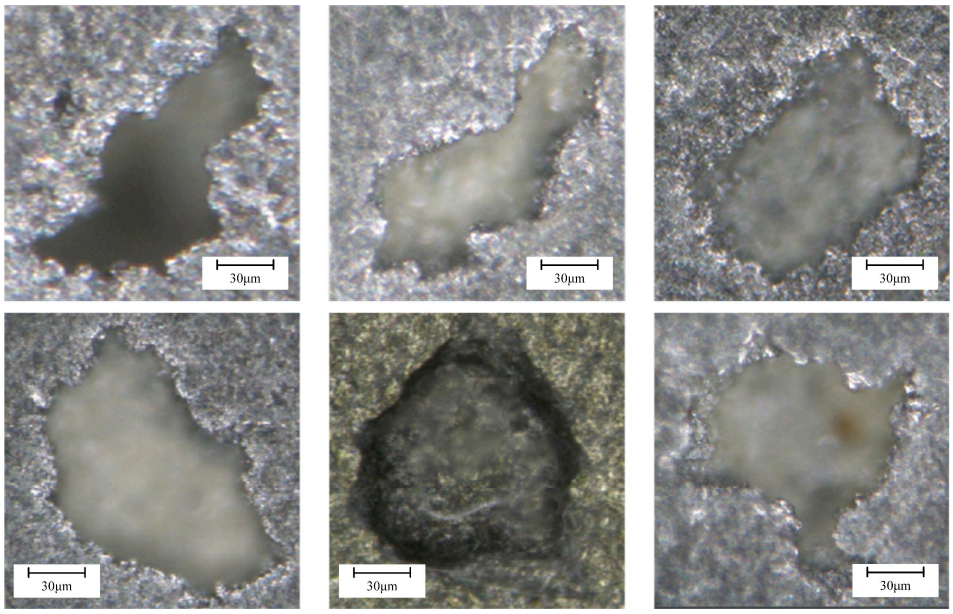


Figure 6. Samples of the defective regions.

The Sobel filter is used to calculate gradient amplitude and direction. The Sobel filters for the x and y directions are as follows:

$$S_x = \begin{bmatrix} -1 & 0 & 1 \\ -2 & 0 & 2 \\ -1 & 0 & 1 \end{bmatrix}, S_y = \begin{bmatrix} 1 & 2 & 1 \\ 0 & 0 & 0 \\ -1 & -2 & -1 \end{bmatrix} \tag{5}$$

Here, S_x denotes the x-direction Sobel filter for detecting edges in the vertical direction. S_y denotes the y-direction Sobel filter for detecting edges in the horizontal direction. If a 3×3 window in the image is A, the gradient value (G) and direction (θ) at pixel C can be calculated using Equation (6):

$$G = \sqrt{G_x^2 + G_y^2}, \theta = \arctan\left(G_y / G_x\right) \tag{6}$$

Here, G_x is the gradient in the x-direction and G_y is the gradient in the y-direction, and G_x and G_y are obtained from Equations (7) and (8):

$$G_x = S_x * A = \begin{bmatrix} -1 & 0 & 1 \\ -2 & 0 & 2 \\ -1 & 0 & 1 \end{bmatrix} * \begin{bmatrix} A_1 & A_2 & A_3 \\ A_4 & C & A_5 \\ A_6 & A_7 & A_8 \end{bmatrix} \tag{7}$$

$$G_y = S_y * A = \begin{bmatrix} 1 & 2 & 1 \\ 0 & 0 & 0 \\ -1 & -2 & -1 \end{bmatrix} * \begin{bmatrix} A_1 & A_2 & A_3 \\ A_4 & C & A_5 \\ A_6 & A_7 & A_8 \end{bmatrix} \tag{8}$$

It should be noted that the symbol $*$ represents the convolution operation. The gradient values and orientations of each pixel can be obtained by sliding the Sobel filter over the image.

After performing gradient computation on the image, the edges extracted based on the gradient values remain blurred. For edges, there is, and should be, only one exact response. Non-maximum suppression is an edge sparsity technique that can help suppress all gradient values other than the local maximum to zero. The gradient of the current pixel is compared with two neighboring pixels in the same direction, and if the gradient of the current pixel is greater than the gradient of the other two pixels, the pixel is retained as an edge point; otherwise, the pixel is suppressed.

After non-maximum suppression, double-threshold filtering was performed. Two thresholds were set, high and low, where pixels above the threshold are considered as strong edges. Pixels below the high threshold and above the low threshold are considered as weak edges. They are set to zero for pixels below the low filtering value. For those considered as strong edge points, they are retained directly. For those considered as weak edge points, it is necessary to determine whether there are strong edge points in their eight connected field pixels; if they are present, the weak edge points are retained, and they are suppressed if they are absent. Finally, the edges can be connected. In addition, the value of the double threshold is uncertain due to the difference in the brightness and contrast of the images in different defect regions. Therefore, edge detection in samples from different defect regions is achieved here by manually adjusting the value of the double threshold. The edge detection results for randomly selected images of the six defect samples are shown in Figure 7. It can be seen that the background region of the original image is rich in the detected edge information, while the defect region is sparse.

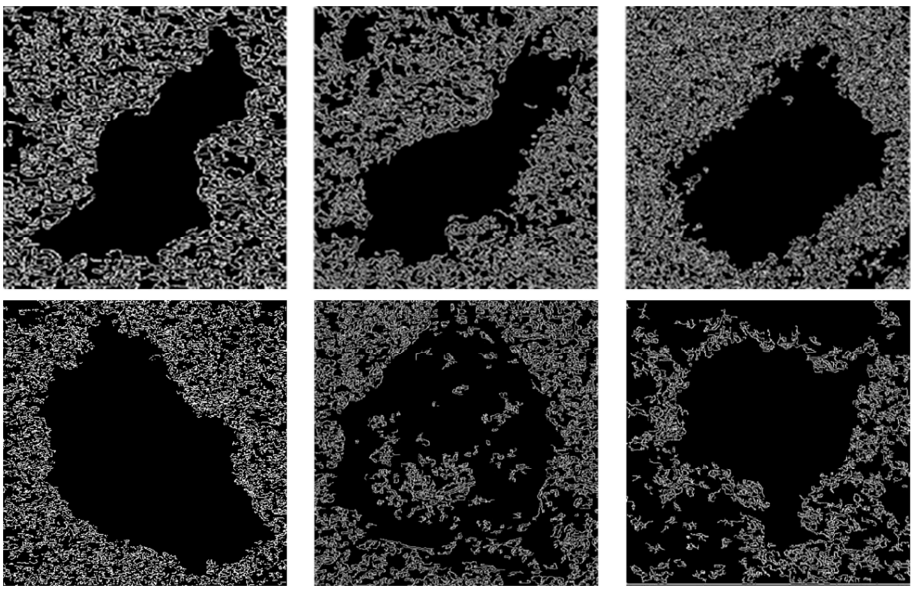


Figure 7. The results of edge detection.

3.2. Morphological Manipulation of Defect Region Images

Morphological manipulation is a highly significant method in image processing and includes operations such as dilation and erosion. After edge detection of the defect region, a binary output image is produced. The defect part is nearly black, and less side information is detected, while the image of the background region is complex and more side information is detected. In order to join the non-defect regions together, a dilatation operation is first

performed so that the non-defect regions are dilated sufficiently to be filled with white. The results for the dilated defect image sample are shown in Figure 8. It can be clearly seen that most of the defect regions in the sample are black and most of the non-defect regions are white. At this point, the defect and non-defect parts of the defect image are roughly separated by two colors, black and white. Since some defect regions are also dilated into non-defect regions during the dilation process, it is necessary to erode the dilated image in order to recover the actual size of the defect and non-defect regions. To avoid excessive erosion, the parameters used for erosion treatment were kept consistent with those used for dilatation. The erosion results are shown in Figure 9, where the defect and non-defect regions have an accurate segmentation line, which facilitates the extraction of the defect profile in the next step.

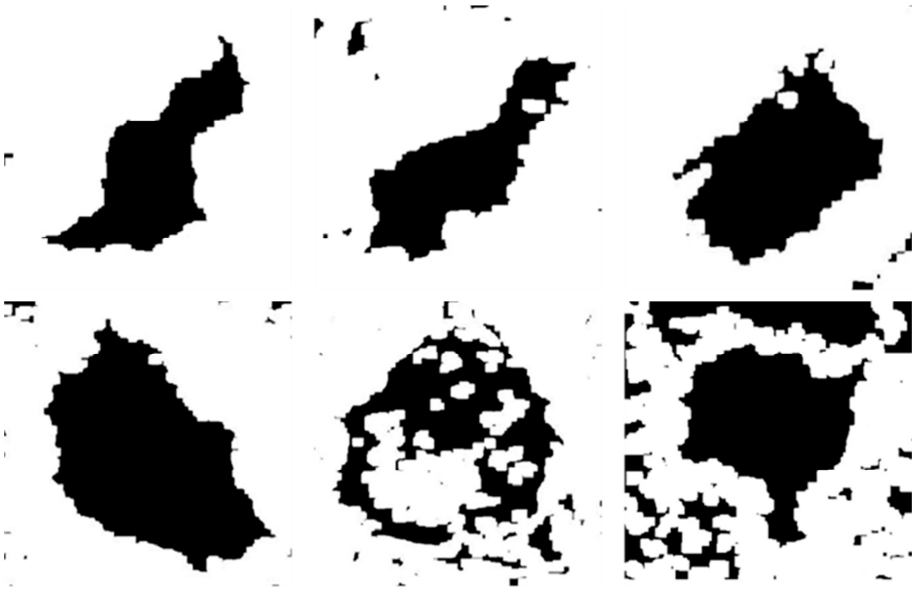


Figure 8. Results of dilation operations.

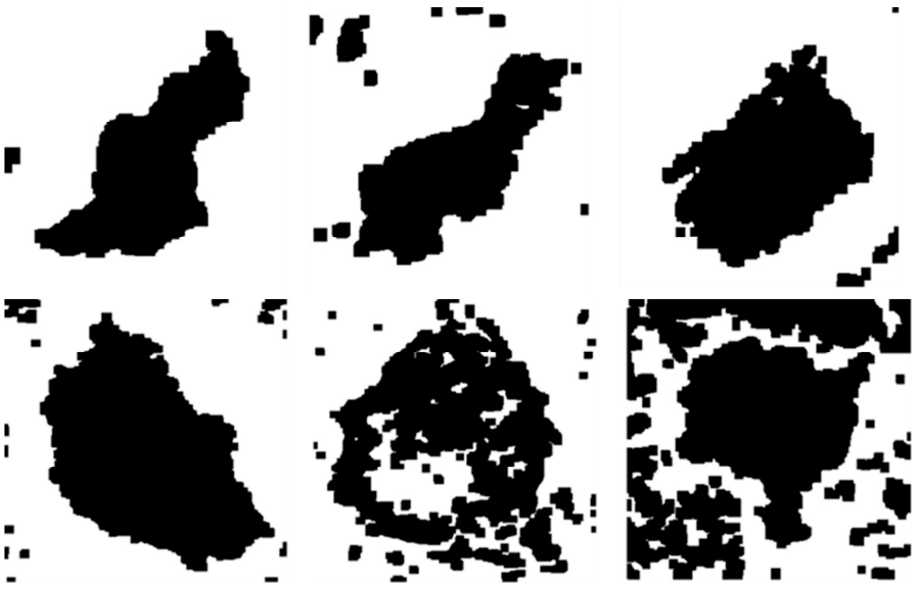


Figure 9. Results of erosion operations.

3.3. Defect Characteristic Parameters

After performing morphological manipulation, there is a more precise dividing line between the defect and non-defect regions; this is the defect profile. From Figure 9, it can be seen that the non-defective region has a small number of small enclosed black regions. In order to filter out these regions, the number of pixels contained within each profile is calculated while extracting the profile. Only the profile containing the highest number of pixels is retained and plotted on the original image, while the number of pixels within the profile is recorded as n_d. Figure 10 shows the extracted defect profiles. In this paper, the area of the defect region (A_d) is selected as the defect characterization parameter, and the calculation method of A_d is as follows:

$$A_d = \left(\frac{d}{n_p}\right)^2 \times n_d \tag{9}$$

Here, d is the actual length of the scale representation, n_p is the number of pixels along the length of the scale, and n_d is the number of pixels in the defect region. The values of d and n_p are directly related to the magnification at the time of image acquisition, and the values of d and n_p at the different magnifications covered are shown in Table 4.

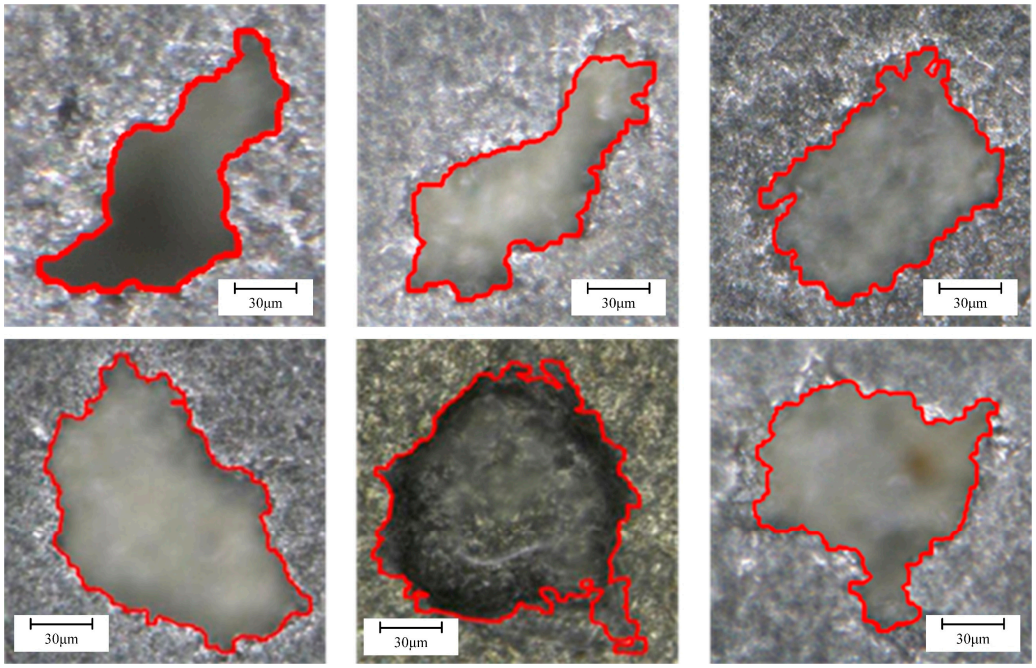


Figure 10. The extracted defect profiles.

Table 4. Values of d and n_p for different magnifications.

Magnifying Power	d (μm)	n_p (Pixel)
100×	100	52
300×	100	148
600×	100	297
1000×	100	476

4. Influence of Machining Parameters on Surface Quality

Based on the detection of surface defects and the extraction of defect characteristic parameters, this section analyzes the effect of machining parameters on the quality of machined surfaces, using the number of defects (N_d) and the total area of defects (A_t) within the same machining area as evaluation criteria. The statistical results for the number

of defects and the total area of defects corresponding to all machining parameters in the same 40 mm area are presented in Table 5.

Table 5. Statistical results for N_d and A_t.

No.	n (rmp)	v_f (mm/min)	a_p (μm)	A (μm)	d (mm)	S_a (μm)	A_t (μm^2)	N_d
1	3000						57,222.57	7
2	6000						53,182.92	9
3	9000	25	10	5	4	54	38,162.55	6
4	12,000						27,794.07	4
5	15,000						11,264.24	2
6		15					18,171.58	3
7		20					25,998.80	4
8	12,000	25	10	5	4	54	27,794.07	4
9		30					26,990.74	4
10		35					50,823.62	5
11			5				19,626.48	3
12			10				27,794.07	4
13	12,000	25	15	5	4	54	17,311.28	3
14			20				28,022.15	4
15			25				39,889.16	5
16				0			39,159.21	5
17				1.25			42,518.35	6
18	12,000	25	10	2.5	4	54	42,178.25	5
19				3.75			27,794.07	4
20				5			22,950.30	3
21					2		18,920.75	2
22	12,000	25	10	5	4	54	27,794.07	4
23					6		37,205.05	5
24					8		34,603.97	4
25						46	23,465.70	3
26	12,000	25	10	5	4	54	27,794.07	4
27						64	31,812.16	4
28						76	49,643.07	6

4.1. Analysis of the Effect of Grinding Parameters

Figure 11 shows the effect of grinding parameters, including spindle speed, feed rate, cutting depth, and ultrasonic vibration amplitude, on the total defect area and the number of defects in the machining region.

From Figure 11a, both A_t and N_d show a significant downward trend with the increase in spindle speed. This is due to the fact that for a given material removal volume, an increase in spindle speed will cause a rise in the number of abrasive grains involved in the cutting zone and, therefore, the cutting volume of individual abrasive grains decreases. This will reduce the cutting force and improve the surface quality. The increase in spindle speed also shortens the effective cutting time of individual abrasive grains, meaning that the heat generated in the shear zone cannot be dissipated in time. A high temperature makes the material softer and easier to process, and this is helpful for improving the surface quality.

Figure 11b shows the effect of the feed rate on A_t and N_d. A_t and N_d are found to increase as the feed rate increases from 15 to 20 mm/min, and then, they remain stable until the feed rate reaches 30 mm/min. The A_t increases significantly when the feed speed is increased from 30 to 35 mm/min. As the feed rate increases, the thickness of the undeformed chips increases, leading to a larger removal volume for a single abrasive grain and therefore resulting in an increase in grinding force. The increase in grinding force leads to an increase in interfacial failure between the silicon carbide particles and the

aluminum alloy matrix, so the silicon carbide particles can be easily broken or pulled out, thus increasing N_d and A_t.

From Figure 11c, it can be seen that the number of defects and the total defect area are in a fluctuating state when the cut depth is increased from 5 to 20 μm. This is due to the fact that at small grinding depths, the increase in grinding depth mainly leads to an increase in the number of flanking abrasive grains involved in the grinding, which does not significantly affect the machined surface quality formed through end-face grinding. After the grinding depth exceeds 15 μm, the number of defects and the total area continue rising until 25 μm. This is because an increased cut depth is less favorable for chip discharging, and the broken silicon carbide particles will cause a secondary cutting of the machined surface, which leads to a decrease in the machined surface quality and larger values of A_t and N_d.

As the amplitude of ultrasonic vibration increases, it can be noticed from Figure 11d that the values of both A_t and N_d show an overall significant decrease. Increasing the amplitude of the ultrasonic vibration increases the dynamic fracture toughness of the SiC particles and the critical depth at which brittle–plasticity transition occurs, so the SiC particles are more likely to be plastically removed or broken into small particles, thereby improving the surface quality.

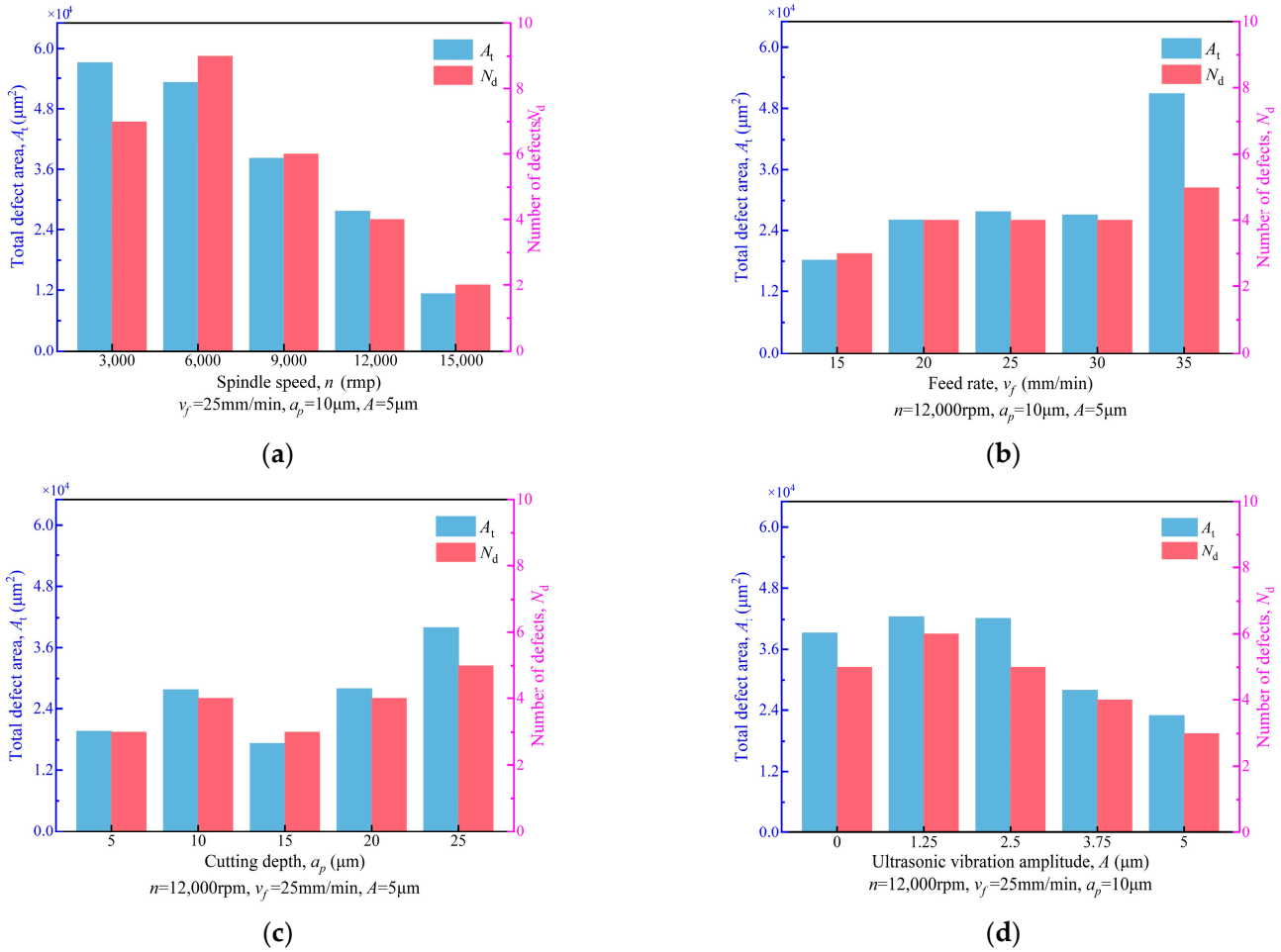
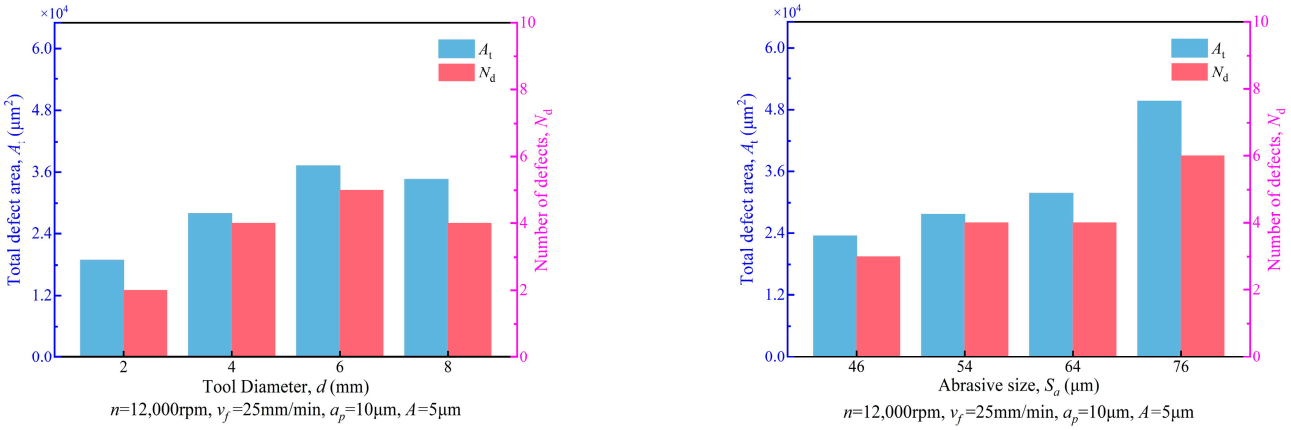


Figure 11. Influences of grinding parameters on A_t and N_d: (**a**) spindle speed; (**b**) feed rate; (**c**) cutting depth; (**d**) ultrasonic vibration amplitude.

4.2. Analysis of the Effect of Tool Parameters

Figure 12 shows the effect of tool parameters on the total area and number of defects in the machining region. Figure 12a shows that for the same machining area, the number of surface defects and the total area of defects increase with the increasing tool diameter. This is due to the fact that as the tool diameter increases, the contact area between the end face of the tool and the machined surface increases, leading to an increase in the cutting force, which reduces the surface quality. The values of A_t and N_d decrease again when the tool diameter exceeds 6 mm. This is because an increase in diameter leads to an increase in the linear velocity of the abrasive grains on the tool, which has the same effect as a high spindle speed, leading to better surface quality. An increase in the size of the abrasive grain results in an increase in the abrasive spacing on the tool. For a single abrasive, this will cause an increase in the thickness of the undeformed chip. This allows a large number of silicon carbide particles to be removed in the form of brittle cracks, resulting in more defects on the machined surface, as shown in Figure 12b.



(**a**) (**b**)

Figure 12. Influences of tool parameters on A_t and N_d: (**a**) tool diameter; (**b**) abrasive size.

5. Conclusions

In this paper, a surface defect detection technique for grinding a SiCp/Al composite has been developed, and a surface quality evaluation criterion based on defect characteristic parameters has been proposed. The conclusions of this paper are as follows:

1. A deep learning-based surface defect detection model is developed for grinding SiCp/Al composites. After training the defect detection model, the average accuracy of the defect detection is 97.4%, and the average detection time for a single image is 47 ms, which meets the requirements for accurate and fast defect detection.
2. OpenCV is used to perform a series of image processing steps such as cropping, edge detection, and morphological operations on the detected defect regions, which achieves the accurate extraction of the characteristic parameters of surface defects. A surface quality evaluation method using the number of defects and the total area of defects in the same machining area as indicators was established.
3. The number and total area of surface defects in SiCp/Al composite grinding increase with the increasing feed rate, tool diameter, and abrasive size, and they decrease with the increasing spindle speed and ultrasonic vibration amplitude. The grinding depth has little effect on the number of surface defects and the total area, as it is less than 20 μm. When it is greater than 20 μm, an increase in the grinding depth leads to a rapid deterioration in the machined surface quality.

Author Contributions: Conceptualization, H.W.; methodology, H.W. and H.Z.; software, H.W.; validation, H.Z.; formal analysis, C.G.; investigation, S.B.; resources, H.L.; experiments, H.W.; writing—original draft preparation, H.W.; writing—review and editing, H.W. and M.Z.; supervision, M.Z.; funding acquisition, M.Z. All authors have read and agreed to the published version of the manuscript.

Funding: This research was funded by the National Natural Science Foundation of China, grant number 51975153.

Institutional Review Board Statement: Not applicable.

Informed Consent Statement: Not applicable.

Data Availability Statement: All data used in this research can be provided upon request.

Acknowledgments: Thanks are due to Wenbo Wang for assistance with the experiments.

Conflicts of Interest: The authors declare no conflict of interest. The funders had no role in the design of the study; in the collection, analyses, or interpretation of data; in the writing of the manuscript; or in the decision to publish the results.

References

1. Ren, S.B.; Qu, X.H.; Guo, J.; He, X.B.; Qin, M.L.; Shen, X.Y. Net-shape forming and properties of high volume fraction SiCp/Al composites. *J. Alloy. Compd.* **2009**, *484*, 256–262. [CrossRef]
2. Sekhar, R.; Singh, T.P. Mechanisms in turning of metal matrix composites: A review. *J. Mater. Res. Technol-JMRT* **2015**, *4*, 197–207.
3. Li, J.G.; Laghari, R.A. A review on machining and optimization of particle-reinforced metal matrix composites. *Int. J. Adv. Manuf. Technol.* **2018**, *100*, 2929–2943.
4. Zhou, J.K.; Lu, M.M.; Lin, J.Q.; Zhou, X.Q.; Guo, M.Q.; Du, Y.S. Investigation of surface integrity transition of SiCp/Al composites based on specific cutting energy during ultrasonic elliptical vibration assisted cutting. *J. Manuf. Process.* **2022**, *79*, 654–665. [CrossRef]
5. Liu, C.; Gao, L.; Jiang, X.G.; Xu, W.W.; Liu, S.N.; Yang, T. Analytical modeling of subsurface damage depth in machining of SiCp/Al composites. *Int. J. Mech. Sci.* **2020**, *185*, 16. [CrossRef]
6. Ge, Y.F.; Xu, J.H.; Yang, H.; Luo, S.B.; Fu, Y.C. Workpiece surface quality when ultra-precision turning of SiCp/Al composites. *J. Mater. Process. Technol.* **2008**, *203*, 166–175. [CrossRef]
7. Zhang, X.; Krewet, C.; Kuhlenkotter, B. Automatic classification of defects on the product surface in grinding and polishing. *Int. J. Mach. Tools Manuf.* **2006**, *46*, 59–69. [CrossRef]
8. Dong, X.H.; Taylor, C.J.; Cootes, T.F. Defect Classification and Detection Using a Multitask Deep One-Class CNN. *IEEE Trans. Autom. Sci. Eng.* **2022**, *19*, 1719–1730. [CrossRef]
9. Girshick, R.; Donahue, J.; Darrell, T.; Malik, J. Region-Based Convolutional Networks for Accurate Object Detection and Segmentation. *IEEE Trans. Pattern Anal. Mach. Intell.* **2016**, *38*, 142–158. [CrossRef] [PubMed]
10. He, K.M.; Zhang, X.Y.; Ren, S.Q.; Sun, J. Spatial Pyramid Pooling in Deep Convolutional Networks for Visual Recognition. *IEEE Trans. Pattern Anal. Mach. Intell.* **2015**, *37*, 1904–1916. [CrossRef]
11. Girshick, R. Fast R-CNN. In Proceedings of the 2015 IEEE International Conference on Computer Vision, Santiago, Chile, 11–18 December 2015.
12. Ren, S.Q.; He, K.M.; Girshick, R.; Sun, J. Faster R-CNN: Towards Real-Time Object Detection with Region Proposal Networks. *IEEE Trans. Pattern Anal. Mach. Intell.* **2017**, *39*, 1137–1149. [CrossRef] [PubMed]
13. Dai, J.F.; Li, Y.; He, K.M.; Sun, J. R-FCN: Object Detection via Region-based Fully Convolutional Networks. In Proceedings of the Annual Conference on Neural Information Processing Systems 2016, Barcelona, Spain, 5–10 December 2016; Advances in Neural Information Processing Systems 29.
14. Redmon, J.; Divvala, S.; Girshick, R.; Farhadi, A. You Only Look Once: Unified, Real-Time Object Detection. In Proceedings of the 2016 IEEE Conference on Computer Vision and Pattern Recognition (CVPR), Seattle, WA, USA, 27–30 June 2016.
15. Liu, W.; Anguelov, D.; Erhan, D.; Szegedy, C.; Reed, S.; Fu, C.-Y.; Berg, A.C. SSD: Single Shot MultiBox Detector. In Proceedings of the Computer Vision–ECCV 2016: 14th European Conference, Amsterdam, The Netherlands, 11–14 October 2016; pp. 21–37.
16. Bochkovskiy, A.; Wang, C.-Y.; Liao, H.-Y.M. YOLOv4: Optimal Speed and Accuracy of Object Detection. *arXiv* **2020**, arXiv:2004.10934.
17. Liao, X.T.; Lv, S.P.; Li, D.H.; Luo, Y.; Zhu, Z.C.; Jiang, C. YOLOv4-MN3 for PCB Surface Defect Detection. *Appl. Sci.* **2021**, *11*, 11701. [CrossRef]
18. Wang, S.; Wang, H.; Yang, F.; Liu, F.; Zeng, L. Attention-based deep learning for chip-surface-defect detection. *Int. J. Adv. Manuf. Technol.* **2022**, *121*, 1957–1971. [CrossRef]
19. Bai, T.; Gao, J.; Yang, J.; Yao, D. A Study on Railway Surface Defects Detection Based on Machine Vision. *Entropy* **2021**, *23*, 1437. [CrossRef] [PubMed]

20. Yue, X.; Wang, Q.; He, L.; Li, Y.; Tang, D. Research on Tiny Target Detection Technology of Fabric Defects Based on Improved YOLO. *Appl. Sci.* **2022**, *12*, 6823. [CrossRef]
21. Liu, Q.; Wang, C.; Li, Y.; Gao, M.; Li, J. A Fabric Defect Detection Method Based on Deep Learning. *IEEE Access* **2022**, *10*, 4284–4296. [CrossRef]
22. Xu, S.; Deng, J.; Huang, Y.; Ling, L.; Han, T. Research on Insulator Defect Detection Based on an Improved MobilenetV1-YOLOv4. *Entropy* **2022**, *24*, 1588. [CrossRef] [PubMed]
23. Qiu, Z.; Zhu, X.; Liao, C.; Shi, D.; Qu, W. Detection of Transmission Line Insulator Defects Based on an Improved Lightweight YOLOv4 Model. *Appl. Sci.* **2022**, *12*, 1207. [CrossRef]
24. Canny, J. A Computational Approach to Edge Detection. *IEEE Trans. Pattern Anal. Mach. Intell.* **1986**, *8*, 679–698. [CrossRef] [PubMed]

Disclaimer/Publisher's Note: The statements, opinions and data contained in all publications are solely those of the individual author(s) and contributor(s) and not of MDPI and/or the editor(s). MDPI and/or the editor(s) disclaim responsibility for any injury to people or property resulting from any ideas, methods, instructions or products referred to in the content.